Journal of Materials Chemistry A

ROYAL SOCIETY OF CHEMISTRY

PAPER

View Article Online
View Journal

Check for updates

Cite this: DOI: 10.1039/d5ta09708h

Separating critical elements from NdFeB magnets with aminophosphonic acid functionalised 3D printed filters and their detailed structural characterisation

Emilia J. Virtanen, [ac] Janne Yliharju, [bce] Esa Kukkonen, [ac] Tia Christiansen,[a] Eero Hulkko, [acf] Minnea Tuomisto,[d] Arttu Miettinen, [bce] Mika Lastusaari, [d] Ari Väisänen[a] and Jani O. Moilanen *[ac]

3D printed filters containing 70 wt% of polyamide (PA) nylon-12 as a polymer matrix and either 30 wt% of a commercial aminophosphonic acid functionalised resin (Lewatit TP260) or a synthesized aminobisphosphonic acid (**1**) as an additive were manufactured *via* selective laser sintering and investigated for the separation of elements from a NdFeB magnet waste. Prior to separation studies, the magnet was leached with 10 v/v% methanesulfonic acid using an S/L ratio of 5 g l^{-1} for 20 h at 60 °C. The PA-TP260 filters adsorbed rare earth elements (REEs) more efficiently than transition and main group elements and showed greater uptake than the PA-**1** filters at the studied pH range of 0.15–4.00. Thus, the PA-TP260 filters were selected for the separation process, wherein Fe was first selectively precipitated from the leachate, while solid-phase extraction was used to separate the remaining elements from the leachate to four distinct fractions: REEs; B, Co; Al; and Cu. Neither significant decrease in the adsorption and desorption percentages of the PA-TP260 filters over 50 adsorption–desorption cycles, nor structural changes, as confirmed by the X-ray tomography and Fourier transform infrared spectroscopy studies, were observed. Overall, the results demonstrate that highly porous and reusable 3D printed filters efficiently separate critical elements from the NdFeB magnet leachate using only eco-friendly solutions of MSA, ammonium chloride, and potassium oxalate, paving the way for greener separation processes for these -critical elements.

Received 27th November 2025
Accepted 8th April 2026

DOI: 10.1039/d5ta09708h

rsc.li/materials-a

Open Access Article. Published on 09 April 2026. Downloaded on 4/30/2026 10:35:07 AM.
This article is licensed under a Creative Commons Attribution 3.0 Unported Licence.

Introduction

Neodymium–iron–boron permanent magnets, commonly abbreviated as NdFeB magnets consist of an alloy mainly made of 60–70 wt% of Fe, 20–30 wt% of Nd, and 0.3–1 wt% of B, as well as 0.5–7 wt% of Pr.[1] Small amounts of other metals such as Al, Ga, Co, Cu, Dy and Tb are added to NdFeB magnets to adjust their properties.[2] For example, Dy and Tb are typically added to increase the coercivity of a magnet at high temperatures.[2,3] The addition of up to 5% of Co increases the Curie temperature of the magnet, a temperature at which the magnet retains its permanent magnetic properties.[4] Ga and Al improve the thermal stability of the magnet.[5] Therefore, the used NdFeB magnets are not only a potential secondary source for rare earth elements (REEs) but also for other critical elements such as Co, Al, or Ga.[6]

Larger-sized wind turbine and electric car magnets can be recycled as they are, but smaller magnets from electric appliances and hard disk drives (HDDs) must be separated from the other components including plastic or metal parts either by manual[7,8] or automatic[9,10] dismantling. After the separation, demagnetisation and grinding of magnets into small particles are typically required before the elements can be separated into their respective fractions by pyro-, hydro-, or solvometallurgical processes.[11] Pyrometallurgical recycling can yield rather pure fractions of REEs.[12,13] However, it requires high temperatures making it an energy-intensive process, although waste heat can be recycled.[14] In hydrometallurgy and solvometallurgy, the elements are typically leached from NdFeB magnets by acidic aqueous solutions or non-aqueous solvents and are then commonly separated from each other by precipitation,[15,16] liquid–liquid extraction,[17] or ion-exchange.[18] So far, the focus in

[a]Department of Chemistry, University of Jyväskylä, P. O. Box 35, FI-40014 Jyväskylä, Finland. E-mail: jani.o.moilanen@jyu.fi
[b]Department of Physics, University of Jyväskylä, P. O. Box 35, FI-40014 Jyväskylä, Finland
[c]Nanoscience Center, University of Jyväskylä, P. O. Box 35, FI-40014 Jyväskylä, Finland
[d]Department of Chemistry, University of Turku, FI-20014 Turku, Finland
[e]School of Resource Wisdom, University of Jyväskylä, P. O. Box 35, FI-40014 Jyväskylä, Finland
[f]Department of Biological and Environmental Sciences, University of Jyväskylä, P. O. Box 35, FI-40014 Jyväskylä, Finland

Open Access Article. Published on 09 April 2026. Downloaded on 4/30/2026 10:35:07 AM. This article is licensed under a Creative Commons Attribution 3.0 Unported Licence.

the literature has been on the separation of the main components of magnets, *i.e.*, Fe, Nd, and Dy, from the simulated NdFeB solutions[19–23] and/or binary solutions containing only the most abundant elements (Fe/Nd or Nd/Dy).[24–29] Using precipitation, 100% pure Nd fraction has been obtained from Nd/Fe[26] and Nd/Dy[28,30] binary systems, and Nd and Co have been successfully separated from the multicomponent solutions containing either Nd, Fe, Co, and Ni, or Co, Nd, and Dy, respectively.[19,20] Recovery of REEs from magnet leachates has been studied by O'Connell-Danes *et al.* who found that the Nd/Pr mixture can be separated from heavier REEs by precipitation and afterwards Dy, Gd, and Ho can be recovered by solvent extraction.[31] Dupont and Binnemans separated Fe from the magnet leachate with ionic liquids, and precipitated REEs and Co with oxalic acid. Co was further separated from REEs by adding ammonia to form soluble Co ammonia complexes resulting in a 99.9% pure REE fraction.[17]

One commonly used ion-exchange material is aminophosphonic acids. These acids contain both an acidic phosphonate group ($PO(OH)_2$) and a basic amine group (NH_2), which make aminomethylphosphonic acids versatile additives for adsorption materials. Aminophosphonic acids can exist as zwitterions, and thus are categorized as polyampholytes, containing both positive and negatively charged moieties.[32] They tend to bind to metals through the phosphonic acid functionality, either ionically to P–OH or covalently to P=O, but the amino moiety can also participate in the binding in an appropriate pH range.[33] Moreover, previous studies have shown that the aminophosphonic acid functionalized ion exchangers adsorb heavy metals and metals with high oxidation states more strongly, in the following order: $Th^{4+} \approx UO_2^{2+} \approx Fe^{3+} > REE^{3+} > Al^{3+} > Cu^{2+} > Co^{+} > Na^{+}$.[34–38] Aminophosphonic acid functionalized commercial ion exchange resins are marketed under commercial names such as MCR50, Purolite S940, or Lewatit TP260. Commercial Lewatit TP260 resin is a macroporous, weakly acidic aminomethylphosphonic functionalised ion exchanger provided in the Na^+ form.[39] Kadous *et al.* studied the sorption of U(IV) to Lewatit TP260 in acetate media and proposed that the uranyl acetate coordinates to either both of the deprotonated OH groups of $PO(OH)_2$ or to a single OH group.[40] Suwannahong *et al.* studied Cu(II) adsorption from e-waste leachate to Lewatit TP260 and suggested Cu(II) binding to both of the acidic $PO(OH)_2$ groups with coordination to the nitrogen atom as well.[41]

3D printed adsorption materials have become increasingly common over the past decade,[42] a trend influenced by advances in 3D printer technology and the ease of manufacturing filters in various sizes, shapes, and with different adsorbents. Typically, an additive is mixed with a polymer matrix, which serves as a framework where the additive can either attach or become encapsulated within the pores of the matrix. The mixture can be printed with different 3D printing techniques, for example, Selective Laser Sintering (SLS),[43–47] Direct Ink Writing (DIW),[48–52] and Digital Light Processing (DLP).[53,54] Porous SLS 3D printed materials have been utilized, for example, in metal recovery,[37,43,47,54–57] analyte preconcentration,[58–60] and organic material capture.[61] Lahtinen *et al.* studied the structure of SLS 3D printed filters containing commercial resin Dowex 21K as an additive with helium ion microscopy (HIM) and X-ray tomography and found out that the porosity of filters was 32% and the additive was attached to the polypropylene matrix but was not encapsulated inside the pores of the matrix.[46] Ibebunjo *et al.* mixed commercial Lewatit MDS TP220 with polypropylene and characterized the SLS printed particles with Scanning Electron Microscopy (SEM), and found that the Lewatit MDS TP220 particles attached to the polymer matrix.[43] Geopolymers have been 3D printed by the DIW technique which has yielded highly organised and controlled structures. Additionally, the porosity of the reported geopolymer materials was reported to be great, over 60% enabling a high area for adsorption.[57,62,63] Porous objects have also been printed with DLP for the adsorption of CO_2 with surface area of up to 40.3 $m^2\ g^{-1}$.[54] While the aforementioned studies demonstrate that porous structures can be obtained using various 3D printing techniques, SLS has been shown to offer distinct advantages. While DIW and DLP require more careful tailoring of the composition of the ink or resin,[64] SLS can utilize commercial polymer powders for essentially any printable additive. Furthermore, the printed objects require no further curing, unlike the ones manufactured with the other two methods. When considering metal recovery, the polymer matrixes used in SLS printing have also been demonstrated to be relatively inert and capable of withstanding strongly acidic metal containing solutions which are commonly used in industrial applications.[37,47,65]

In this work, we present the recovery of various elements from NdFeB magnets using two types of 3D printed filters. These filters contain polyamide (PA) nylon-12 as the polymer matrix and either commercial Lewatit TP260 (PA-TP260) or synthesized aminobisphosphonic acid **1** (PA-**1**) as an additive. The 3D printed filters were thoroughly characterized with X-ray tomography, Fourier transform infrared spectroscopy (FTIR), X-ray powder diffraction (PXRD), and, for the first time, scanning near-field optical microscopy (SNOM). These complementary characterization techniques provided insight into their composition, morphology down to the nanometer scale, and the attachment of the additive, which seem to vary from one additive to another. Furthermore, adsorption behaviour was systematically evaluated for a series of PA-TP260 filters containing different amounts of TP260, and adsorption isotherms were obtained for each composition, revealing how the amount of additive influences the metal uptake. 50 adsorption–desorption cycles were also conducted to demonstrate long term reusability of PA-TP260 filters. Such detailed studies have not been previously reported for aminophosphonic acid based 3D printed filters, although the good performance of PA-**1** filters in REE recovery from mining wastewater has been demonstrated.[37] Methanesulfonic acid (MSA), which is a greener alternative for the commonly used mineral acids like HCl, HNO_3 and H_2SO_4, was used in both the leaching of magnets and as the acid background of recovery studies. Although the good leaching and acid background properties of MSA have been reported before in the recovery studies focusing on other secondary sources,[66–70] these properties of MSA have not yet been utilized in the recovery studies of NdFeB magnets to the

 This journal is © The Royal Society of Chemistry 2026

Open Access Article. Published on 09 April 2026. Downloaded on 4/30/2026 10:35:07 AM. This article is licensed under a Creative Commons Attribution 3.0 Unported Licence.

best of our knowledge. Herein we show that by combining the reusable 3D printed filters with ecofriendly MSA, ammonium chloride, and potassium oxalate solutions, all the elements in the studied NdFeB magnet can be separated into their own less complex fractions. In particular, a very pure REE fraction with the purity of 99.4 ± 0.4% is obtained. Four other fractions containing majority of B, Al, Co, and Cu can be obtained for further separation.

Results and discussion

Preparation of the 3D printed filters

Nylon-12 (polymer matrix) and two different additives, namely Lewatit TP260 and dodecylaminobisphosphonic acid **1**, were used in the 3D printing of the PA-TP260 and PA-**1** filters, respectively. Nylon-12 was selected as the polymer matrix because it was almost completely inactive towards metals in a NdFeB magnet solution without the additives (Table S1). The PA-TP260 filters were prepared by mixing 5, 10, 20, 30, 40, or 50 wt% of the finely grounded TP260 with commercial nylon-12 powder and the resulting mixtures were used for the 3D printing. The filters containing ≤30 wt% of TP260 were robust and durable, but when the amount of TP260 was increased over 40 wt%, the filters started losing their mechanical durability. Thus, most of the studies were carried out for the 30 wt% filters and the abbreviation PA-TP260 refers to a filter with 30 wt% of TP260 unless stated otherwise. The PA-**1** filters consisting of 30 wt% of **1** and 70 wt% of nylon-12 were manufactured as previously reported.[37] All 3D manufactured filters were 5 mm thick with a diameter of 16.6 mm and they were prepared using a ShareBot SnowWhite SLS 3D printer. Each filter was cleaned thoroughly with deionized water to remove any unsintered powder before further studies.

Characterisation of a 3D printed filter

FTIR, PXRD, X-ray tomography, and SNOM were applied to characterize the PA-TP260 filters. For PA-**1**, PXRD and FTIR characterization has been reported before.[37] According to the measured FTIR spectra of nylon-12, TP260 and PA-TP260, the additive (TP260) was proved to stay intact in the filter after the 3D printing process (Fig. S1). This was further confirmed using the PXRD although the peaks arising from TP-260 were broad due to its amorphous nature (Fig. S2).

X-ray tomography and image analysis were applied to characterise the morphology of the PA-TP260 filter at the micrometer level. In addition to the printed filter, a PA-TP260 powder sample was imaged, and the particle size distribution of the powder was measured. In both cases, the isotropic voxel size was 6.6 μm (voxel refers to a 3D pixel). For the PA-TP260 filter, the measured total porosity was 50 ± 2%, and the average pore size was 34 ± 5 μm (Fig. S3). The estimated standard deviation of the pore size was 13 ± 2 μm. Previously reported values for PA-**1** are 59 ± 2% (total porosity), 95 μm (average pore size), and 50 μm (the standard deviation of the pore size), which indicate that small deviations are observed between the parameters of PA-**1** and PA-TP260.[37] Only approximately 0.01% of the pores inside the printed material are not connected to the air outside the sample. Furthermore, the measured surface area of the printed filter was 221 ± 10 cm^2 in the analysed volume, leading to a specific surface area of approximately 0.12 $m^2\ g^{-1}$. However, the measured specific surface area is strongly dependent on the imaging resolution, and therefore, this value will underestimate the surface area, *e.g.*, available for the adsorption process.

The particle size distributions for the printed filter and powder sample are presented in Fig. S4. Most particles are smaller than approximately 150 μm, but a small number of larger particles are also present, ranging from 150 μm to 400 μm. Additionally, the mode of the distribution was 65 ± 5 μm for both cases (powder and printed). The average particle sizes were 69 ± 5 μm for the printed material and 64 ± 5 μm for the powder. The distributions indicate a trend of increasing particle size during the printing process. This likely results from misinterpreting connected particles as a single larger particle, although the segmentation process aims to separate and identify particles individually, even when they are touching. According to the information given by the supplier of nylon-12 (Materflow Oy), 80% of the particles have sizes ranging from 40 μm to 90 μm (the size of 50% of the particles is approximately 58 μm), and the particle size of the Lewatit TP260 before powdering was approximately 400 μm.[39] Therefore, the results of the image analysis were plausible. In addition to numerical characterisation results obtained based on image analysis, the structure of the PA-TP260 filter was visually studied, and the additive was found to be uniformly distributed throughout the filter (Fig. S5).

Concerning the accuracy of the results, it is essential to note that the image analysis results describe the characteristics of the pores and particles within the spatial scale determined by the spatial imaging resolution. To examine the structure more closely, small volumes (approximately 1 mm × 1 mm × 1 mm) of both PA-TP260 and PA-**1** filters were imaged using an isotropic voxel size of 0.6 μm. Cross-sections from these high-resolution 3D tomography images are shown in Fig. 1. The images reveal that the additives (lighter parts) are attached to nylon-12 particles (darker parts), most likely due to the partially melted surfaces of the particles during SLS 3D printing.

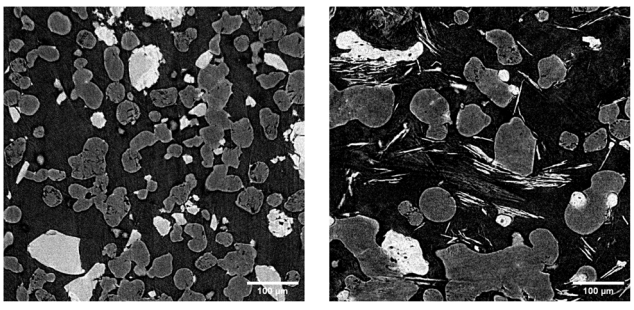

Fig. 1 High-resolution tomographic cross-sections of the PA-TP260 (left) and PA-**1** (right) filters. These data were not used in the image analysis, but were used to visually study the micrometre-level structure with an isotropic voxel size of 0.6 μm. The darker areas represent the nylon-12 particles, while the lighter areas represent the additives.

Open Access Article. Published on 09 April 2026. Downloaded on 4/30/2026 10:35:07 AM.
This article is licensed under a Creative Commons Attribution 3.0 Unported Licence.

Additive particles were generally not embedded in the pores of the nylon-12 matrix. While some small particles may appear encapsulated, the limited spatial resolution does not reveal all the porosity, which could create flow paths toward the additives. Thus, the structures are similar to what have been observed in other SLS 3D printed filters with different additives and polymer matrices.[43,46] Furthermore, most of the surface of an additive particle is not in contact with another particle (especially in PA-TP260). In some instances, a particle may seem disconnected from others, but this is because Fig. 1 is a 2D cross-section of a 3D volume. In the case of PA-TP260, one can notice that additive particles are parts of spheres (the initial shape of the TP260). In contrast, in PA-**1**, the additives are partially present in a plate-like structure, as previously observed when the PA-**1** filters were studied using HIM.[37] It also seems that **1** is more firmly attached in the nylon-12 matrix than TP260, likely due to the lower melting point (close to the laser temperature) of **1** compared to TP260.

To get more insight into these results, nano-FTIR[71,72] measurements were performed on single particles collected from PA-**1** and PA-TP260 filters, as well as on pure 3D printed nylon-12 for reference. The measured area was chosen to be from 1800 cm^{-1} to 1000 cm^{-1} as characteristic P–O peaks can be detected at 1156 cm^{-1} for the additives **1** and TP260. The nano-FTIR spectral measurement positions are shown in Fig. S6, and the spectra presented for the particles are an average of different measurements of each particle (Fig. 2). In the case of PA-**1** particle, it was shown that the additive **1** is coating the nylon-12 particle as a strong P–O peak can be detected at 1170 cm^{-1}, which is slightly shifted compared to the peak observed in the FTIR spectrum of the bulk material. The nylon-12 particle measured for the reference also showed peak shifting from 1635 cm^{-1} to 1645 cm^{-1}. For PA-TP260, the measured particle exhibited a P–O peak around 1156 cm^{-1}, but no characteristic C=O peak associated with nylon-12 was detected. This finding suggests that TP260 and nylon-12 particles are less strongly bound together compared to nylon-12 and PA-**1**, further supporting the results from the X-ray tomography analysis.

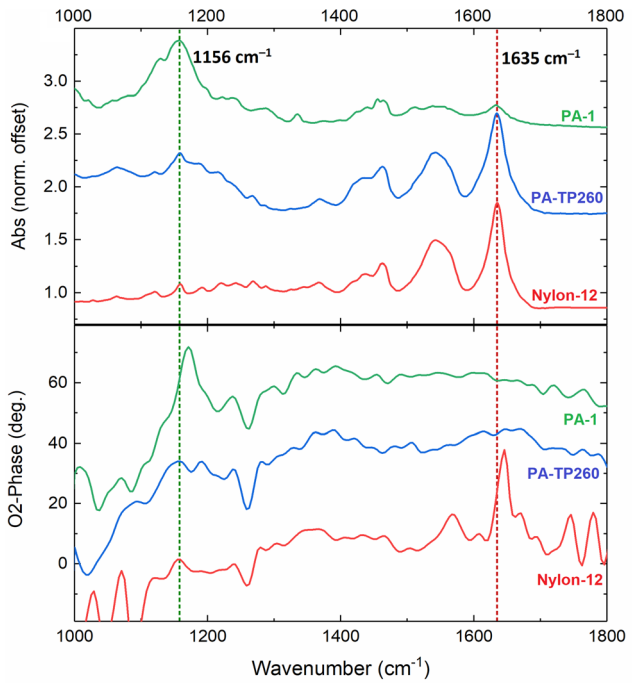

Fig. 2 FTIR-spectra for the bulk material (top), and spectra for the single particles measured using SNOM (down).

Leaching of the NdFeB magnet

The elemental composition of the NdFeB magnet was determined by total acid digestion with aqua regia and an S/L ratio of 5 g l^{-1}. The total dissolution time for the magnet was 3 h at 60 °C, and no residues were detected after filtration. The amount of leached elements was determined using ICP-OES (Table S2). The main components were Fe (63 wt%) and Nd (21 wt%), followed by Pr (6 wt%), Dy (3 wt%), and B (1 wt%). The magnet also contained small amounts of Al, Co, Cu, Sm, Tb, and Ho (<1 wt%).

The efficiency of MSA in leaching the NdFeB magnet was studied across various concentrations of MSA ranging from 10 vol% to 100 vol%. The leaching temperature (60 °C), time (20 h), and S/L ratio (5 g l^{-1}) were kept constant. The 10–60 vol% and 90–100 vol% MSA solutions efficiently leached the elements, except Cu, from the magnet, but the leaching efficiency significantly decreased in the solutions containing 70 vol% and 80 vol% of MSA (Fig. 3). The decrease in the leaching efficiency can partially be explained by the low solubilities of metal salts in the concentrated MSA solutions.[73] For example, the leaching efficiency of MSA has been reported to decrease for Zn,[73] Fe,[73,74] and the red phosphor (YOX; Y_2O_3:Eu^{3+})[66] with the increasing concentrations of MSA. However, in this study, the above explanation is only valid for the dip region between 70 vol% and 80 vol% solutions, as the 90 vol% and 100 vol% solutions leached the metals similarly to the 60 vol% solution. A similar dip in the leaching efficiency of MSA has previously been reported for the halophosphate phosphor (HALO; $(Sr,Ca)_{10}(PO_4)(Cl,F)_2$:$Sb^{3+}$,$Mn^{2+}$).[66] It was attributed to the formation of unstable calcium complexes in

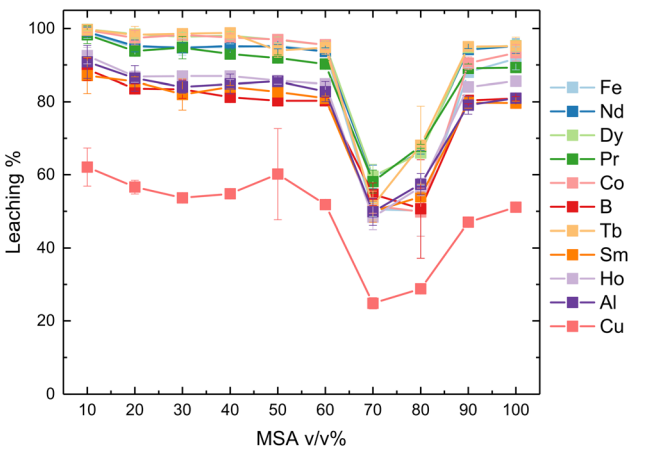

Fig. 3 Leaching NdFeB magnet with different v/v% MSA at 60 °C for 20 h.

This journal is © The Royal Society of Chemistry 2026

Open Access Article. Published on 09 April 2026. Downloaded on 4/30/2026 10:35:07 AM.
This article is licensed under a Creative Commons Attribution 3.0 Unported Licence.

the dip region, whereas in higher concentrations, more soluble calcium methanesulfonates are formed. Interestingly, no clear Fe precipitation was observed during the leaching experiments in regions of 10–60% and 90–100%, as reported in previous studies.[73,74] This may be because Fe is not fully oxidized to the +3 state during the leaching process (see below).

Given that MSA completely leached most of the studied elements, its leaching efficiency is comparable to or better than that of previously investigated acids. For example, ~90–100% leaching of Nd and Fe from NdFeB magnets has been achieved with H_2SO_4 (ref. 75) and acetic acid,[16,76] depending on the molarities of the acids and leaching conditions. Furthermore, a selective 90% leaching of REEs has been reported for 1 M HNO_3 in an autoclave at 60 °C.[77] Although the leaching efficiency of MSA towards REEs has been investigated with the lamp phosphor waste,[66] its efficiency with NdFeB magnets has only been tested for Co.[78] Notably, 1 M MSA at 70 °C dissolved 100% of Co from the NdFeB magnet, similar to the results obtained here.

Iron precipitation

Because Fe is the major element in the NdFeB magnet leachate, its precipitation from the leachate simplifies the recovery and separation of other metals in the subsequent solid-phase extraction step. The oxidation state of Fe should be (II) after the MSA digestion due to the non-oxidizing nature of MSA, as has been reported before for other non-oxidizing acids.[16] The complete precipitation of Fe(II), however, requires a pH of 9.5,[79] which is an unviable option due to the co-precipitation of other elements under such basic conditions.[80] Therefore, the oxidation of Fe(II) to Fe(III) is necessary for the successful precipitation at lower pH values. The oxidation was carried out by adding an equivalent amount of 30% H_2O_2 to the solution, and raising the pH to 3.7 with 25% NH_4OH.[81] During the oxidation process, a brown precipitate formed, which was removed by filtration. The absence of Fe in the filtrate was confirmed by ICP-OES measurement. Only traces of Fe were detected in the filtrate, and the obtained precipitation percentage for Fe was 99.9%, indicating complete removal of Fe from the magnet leachate. Only Al (27% ± 3%) and Cu (12% ± 7%) co-precipitated clearly with Fe during the oxidation process, whereas the precipitation of other elements was less than 5% (Table S3).

Adsorption studies

Adsorption tests were performed for the three stacked PA-**1** and PA-TP260 filters, and each test was done in triplicate. In the tests, 40 ml of the Fe-free MSA leachate of NdFeB magnets was injected through the filters with a flow rate of 90 ml h^{-1}. The tests were first performed at two different pH values, which were 0.15 and 4.0. The former is the pH of 5% MSA, and at the latter pH, the deprotonation degree of the additives increases.[82,83] At both pH values, the PA-**1** filters adsorbed each element substantially less than the PA-TP260 filters (Fig. 4 and S7). As seen in Fig. 4, the PA-TP260 filters adsorbed over 90% of REEs but no significant amount of other elements at pH 0.15. This can likely be attributed to the interplay between ionic radius, coordination number,

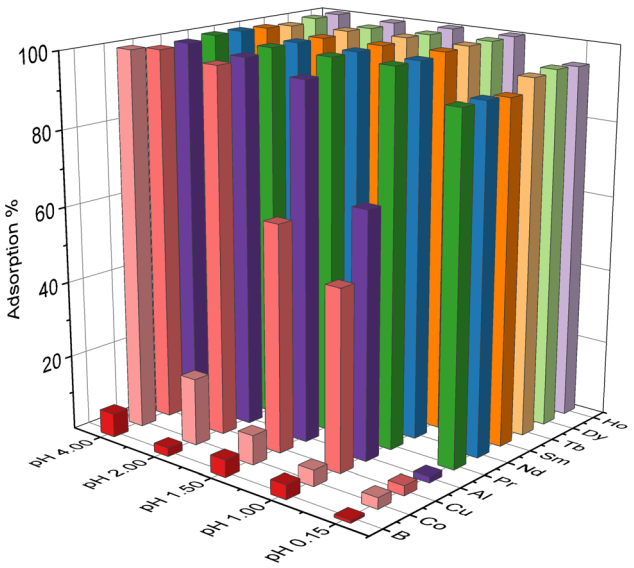

Fig. 4 Adsorption percentage as a function of pH 0.15–4.00 for the PA-TP260 filters.

Lewis acidity and oxophilicity. REEs with larger ionic radii typically prefer higher coordination number and exhibit stronger oxophilicity than Al, Cu, or Co.[84–89] Thus, REEs form more stable complexes with aminophosphonates in PA-TP260 even though the effective Lewis acidities of Al, Cu and Co are similar in strength. For the PA-**1** filters, at this pH, the adsorption percentages of all elements were 10% at maximum (Fig. S7). This is in line with the previous study, because the PA-**1** filters showed low uptake of REEs under strongly acidic conditions (pH ≤ 2).[37] At pH 4, the PA-**1** filters adsorbed less than 50% of REEs, Cu, and Al, while the PA-TP260 filters completely adsorbed all elements except B. The low adsorption for B is likely due to its existence as $B(OH)_3$ under acidic pH conditions, rather than as a free cation, and therefore cannot participate in cation-exchange or chelation.[90] The results obtained here are similar to what Hermassi *et al.* previously reported for TP260, with the exception that they observed 20% of Co adsorbing at pH 0, which likely results from the different acid background (H_2SO_4).[35] The results indicate that the REEs can be separated from B, Al, Co, and Cu at pH 0.15 using the PA-TP260 filters, whereas the PA-**1** filters are rather ineffective in these concentrations. The better uptake of PA-TP260 filters compared to that of the PA-**1** likely stems from TP260's polymeric structure, in which phosphonate groups are immobilized in proximity within an organized matrix.[91,92] This prearranged environment can enhance metal uptake from the magnet solution. In contrast, PA-**1** consists of discrete aminobisphosphonate molecules and therefore does not provide as highly preorganized coordination environment as PA-TP260. The PA-TP260 filters also separate B from other elements at pH 4.

Due to the better performance of the PA-TP260 compared to the PA-**1** filters, a more accurate pH screening was only performed for the PA-TP260 filters to find out the optimal pH range for better separation of all elements. Three additional pH values, 1.0, 1.5, and 2.0 were tested. At pH 1.0, the adsorption of B and Co

Open Access Article. Published on 09 April 2026. Downloaded on 4/30/2026 10:35:07 AM. This article is licensed under a Creative Commons Attribution 3.0 Unported Licence.

remained low (~4%), whereas 48 ± 5% of Cu, 65 ± 8% of Al, and all the REEs were adsorbed by the filters. When the pH was adjusted to 1.5, and subsequently to 2.0, the adsorption of Al was observed to increase to 95 ± 4% and 98 ± 3%, respectively. For Cu, the increases were 60 ± 10% and 97 ± 2%. Although the adsorption of Al was almost complete at pH 2, the co-adsorption of Co was also significantly greater (17%) compared to pH 1.5 which was not aimed for. Therefore, pH 1.5 was deemed to be the best pH for separating Al and Cu from B and Co once the REEs were separated from all other elements at pH 0.15.

Adsorption–desorption cycles

The reusability of the filters and their possible structural changes associated with the adsorption and desorption steps were investigated by performing 50 subsequent adsorption–desorption cycles for one PA-TP260 filter. Only one filter was selected because an X-ray tomography image was taken from that filter every tenth step of the cycles. Importantly, its adsorption and desorption capacity were within the standard deviation (Table S4) of those observed for three stacked filters (Table S5), validating the results obtained only for one filter. In each adsorption–desorption step, 9 ml of simulated NdFeB solution was injected into the filter at pH 0.15 with a flow rate of 90 ml h^{-1}, followed by the elution of the filter with MSA with a flow rate of 15 ml h^{-1}. According to the initial test, 3 M MSA was used as an eluent in the first five cycles, but it was shortly noticed that better desorption of elements is obtained with 5 M MSA. Indeed, the additional desorption tests performed for a different set of filters showed that 5 M MSA desorbs the REEs better than 3 M MSA (Fig. S8). 6 M HNO_3 was also tested as an eluent because it was previously shown to elute Nd from the PA-**1**,[37] however, it performed poorly at eluting heavy REEs (Dy, Tb, and Ho) from PA-TP260 compared to MSA.

As seen in Fig. 5, a small decrease in the adsorption efficiency was observed after the first 15 cycles, but otherwise it remained almost invariable during the 50 cycles. It even slightly increased at the end of the cycles. Desorption of the elements was also very efficient except in the first five cycles when 3 M MSA was used as an eluent instead of 5 M MSA. Only a small amount of heavier REEs accumulated in the filter during the process, as indicated by the residual amount of elements present in the filter (Fig. S9). After completing the 50 cycles, an IR spectrum was measured by scratching a small amount of the material from the bottom of the filter, and no deterioration was observed. The small detectable changes arise from metals coordinating to the TP260 functional sites (Fig. S10), which are discussed in more detail in the following chapter. 50 or over 50 cycles have been performed before for adsorbent materials[93] in adsorption–desorption studies, but usually much more less cycles are performed.[43,59,94–96] Concerning this, the 50 adsorption–desorption cycles truly highlight the reusability of the PA-TP260 filters. Also, the adsorption efficiency of adsorption materials can decrease from 100% to nearly 60% even after five cycles, as reported for the 3D printed adsorbent in the adsorption of Cu.[43] A similar, though less pronounced, decrease has also been reported for an ion-imprinted silica, where the adsorption of Dy decreased from 100% to 81% within five cycles.[95] This kind of behaviour was not observed for the PA-TP260 filter within five cycles, but it performed similarly to the previously reported aminophosphonate sorbents, which adsorbed 95% of Nd after six cycles.[94]

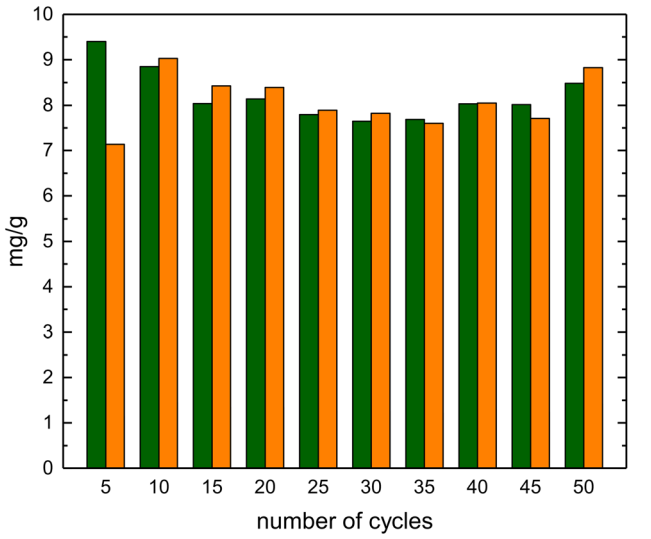

Fig. 5 Amounts of adsorbed (green) and desorbed (orange) elements in mg during the 50 adsorption–desorption cycles.

A total of six tomographic scans were performed during the 50 adsorption–desorption cycles. The first scan was conducted at the initial stage after the filter was prepared. Subsequent scans were conducted every ten cycles to assess changes in total porosity, pore and particle size distributions, total surface area, and connected porosity. The size of the volume under study was the same in every 3D image, and its location was visually matched in each step. The images essentially covered the same part of the studied filter (as also illustrated in the features of the depth profiles of the porosity in Fig. S11). Considering the uncertainties in the results, no significant changes were observed in the global averages of any of the measured properties (Table S6). The depth profiles of the porosity and pore size distributions (Fig. S11 and S12) also show overall minor changes. However, at the end state (after 50 cycles), there is a slight increase in the number of smaller pores compared to other states, and there is also a slight decrease in local porosity with depth in the studied volume. These observations suggest some minor local structural changes. However, due to uncertainties in the measurements (2 percentage points for porosity), the changes are not significant. These findings, along with adsorption–desorption cycles, provide robust evidence for the reusability of the filters, supporting their utilisation in industrial recovery processes.

Adsorption mechanism

To get more insight into the adsorption mechanism, the PA-TP260 filter saturated with Nd was characterized using FTIR and X-ray tomography. At the molecular level, the adsorption of Nd to an aminophosphonic acid moiety can occur *via* different

 This journal is © The Royal Society of Chemistry 2026

Open Access Article. Published on 09 April 2026. Downloaded on 4/30/2026 10:35:07 AM.
This article is licensed under a Creative Commons Attribution 3.0 Unported Licence.

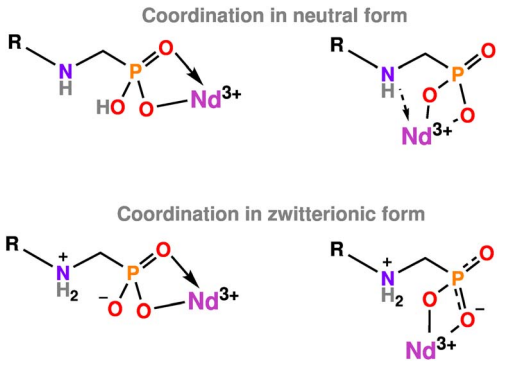

Fig. 6 Possible coordination modes of Nd^{3+} to the aminophosphonic acid moiety in the neutral (above) and zwitterionic (below) form.

coordination modes as illustrated in Fig. 6.[83,97,98] It has been reported that an acid anion, MSA anion in this case, can protonate the NH moiety, leading to the salt formation ($NH_2^+CH_3SO_3^-$).[35] Therefore, the coordination of a metal ion likely only occurs in the phosphonic acid moiety at low pH values,[99] whereas at higher pH values, the coordination to neutral amine is possible.[100]

When the FTIR spectrum of the unused PA-TP260 was compared to the one saturated with Nd, it was found that the peaks associated with nylon-12 remained unchanged as expected, but changes in the peaks arising from the phosphonate moiety were observed (Fig. 7). The asymmetric and symmetric P–O_3 stretches at 1156 cm^{-1} and 1064 cm^{-1} shifted to 1158 cm^{-1} and 1040 cm^{-1}, respectively. The P–O_3 bend at 541 cm^{-1} shifted to 551 cm^{-1} upon coordination of Nd. Sahni *et al.* reported that the zwitterionic structure is retained after coordination if only minimal changes are observed in the asymmetric P–O_3 stretch.[99] The most noticeable changes were observed for the P–OH stretch at 924 cm^{-1}, which shifted to 943 cm^{-1} with a significant decrease in intensity. All these observations indicate that Nd coordinates to the phosphonic acid group, and in particular to the P–OH moiety, retaining its zwitterionic structure. The peaks arising from the C–S stretch and the S–O deformation[101] vibrations of MSA at 771 cm^{-1} and 523 cm^{-1}, respectively as well as the S–O_3 stretches[102] at 1158 cm^{-1} and 1040 cm^{-1} indicate that MSA anion(s) most likely complete the coordination sphere of Nd ion. The appearance of the peak at 1216 cm^{-1} either arises from a coordinating MSA or a trapped MSA–H_2O adduct inside the filter.[103] Unfortunately, FTIR spectra do not reveal anything about the HN···Nd coordination as the characteristics of the nylon-12 matrix mask all possible shifts. The problem has also been observed before, however, if the phosphonic acid exists as a zwitterionic form, it is unlikely that the NH_2^+ moiety participates in coordination.[99,104]

To confirm the adsorption of Nd to the additive at the microscale, a filter was imaged with X-ray tomography before and after the Nd adsorption, and then the voxel values of the 3D images were compared. The tomographic reconstruction yields the values of the linear attenuation coefficient, which depend on the energy, density, and elemental composition of the

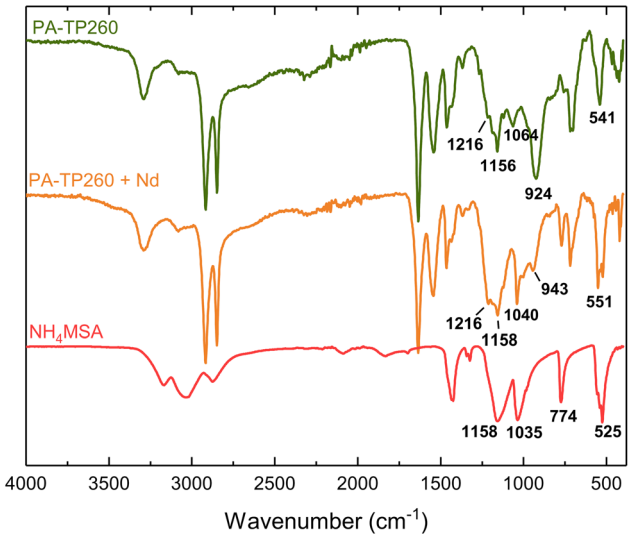

Fig. 7 FTIR spectra of the unused PA-TP260 filter (green), PA-TP260 filter saturated with Nd (red), and ammonium salt of MSA (grey).

sample. Therefore, the local values of the linear attenuation coefficients change during the adsorption of Nd. However, in practice, the result of the reconstruction is the so-called effective attenuation coefficient, which is not the true material property but depends on several factors, *e.g.*, the camera's response, beam hardening effect (corrected here with the polynomial method[105]), and scattering of X-rays. It was evaluated whether the measurement accuracy was sufficient to observe the introduction of Nd into the filter structure. To this end, the distributions of the attenuation coefficient values before and after Nd adsorption were compared, as shown in Fig. 8. The first peak at −1.0–0.0 corresponds to the air inside the filter, the second peak around 1.0–2.0 corresponds to nylon-12, and the third weak peak corresponds to the additive. There are small systematic differences in the positions of the air and nylon peaks due to differences in imaging conditions (*e.g.*, source and detector stability). However, the change in the peak corresponding to the additive is evident and caused by the increase in density due to Nd. Thus, it can be concluded that the introduction of Nd into the structure is well visible in the distribution of attenuation coefficient values. Fig. 8 also includes a visualisation where the voxels corresponding to the additive and Nd are coloured red. The selection of a lower threshold, here 3.0, for visualisation, is a rough estimate, which introduces some uncertainties in interpretation. However, the overall trend is clear; Nd is only found in the additive particles, and only a negligible amount might remain in nylon-12 particles. The result is fully in line with adsorption tests performed for the pure nylon-12 and the PA-TP260 filters (see above). Additionally, the height of the nylon-12 peak in Fig. 8 increased after the adsorption of Nd, indicating a higher concentration of nylon-12 particles in the studied volume. However, this increase is not related to the adsorption process but most likely to the moisture in the surrounding air and the minor shrinking of the filter.

Open Access Article. Published on 09 April 2026. Downloaded on 4/30/2026 10:35:07 AM.
This article is licensed under a Creative Commons Attribution 3.0 Unported Licence.

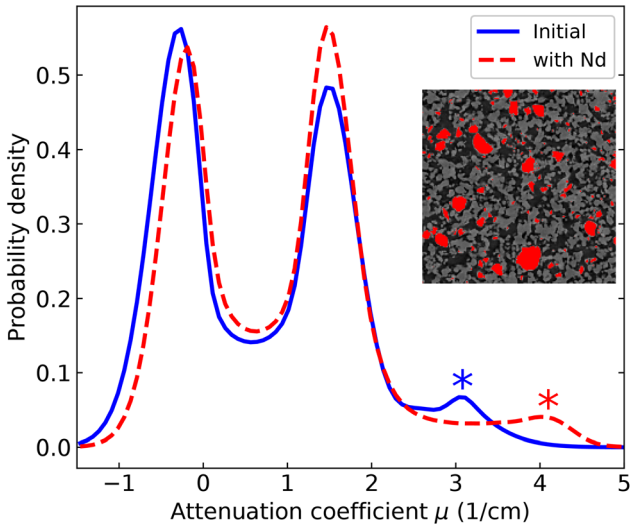

Fig. 8 Distributions of the attenuation coefficient values before (blue) and after adsorbing Nd (red). The inset figure highlights the TP260 particles that are saturated with Nd. The asterisks indicate qualitatively the attenuation coefficient values corresponding to the TP260 particles.

Adsorption isotherms

The effect of the wt% of TP260 on the adsorption efficiency and mechanism of the PA-TP260 filters was investigated by fitting the adsorption isotherms of Nd to the Langmuir (monolayer adsorption),[106] Freundlich (multilayer adsorption),[107] and Sips (a combination of Langmuir and Freundlich models)[108] models. All isotherm experiments were performed in triplicate by passing 10 ml of 50–1000 mg per l Nd solution in 5% MSA through one filter containing 5 wt% to 50 wt% of TP260 at a flow rate of 90 ml h^{-1}. The adsorbed amount of Nd was determined using ICP-OES. Q_m was calculated with respect to the mass of the filter and the amount of TP260 in the filter. The filters containing 10–30 wt% of TP260 fitted best to the Langmuir model, whereas filters containing 40 wt% and 50 wt% of TP260 followed Freundlich adsorption isotherms (Table S7 and Fig. S13–18). Interestingly, the 5 wt% PA-TP260 filter fit well only to the Sips model. Given that the filters contain the same adsorbent (TP260), the adsorption mechanism at the molecular level should be identical for all filters, but the isotherm results indicate differences on a larger scale. However, the adsorption mechanism (here mono- *vs.* multilayer) cannot always be supported only by the curve fitting.[109] Controversial results have also been reported before, for example, for the adsorption of La^{3+} by Lewatit TP260.[110–112] Similarly to this study, the isotherms of La^{3+} fit well to both the Langmuir and Freundlich models. For this reason, the primary purpose of the isotherm analysis in this work is to compare the adsorption capacities of filters with different wt% amounts of TP260, rather than to interpret adsorption mechanisms.

The maximum adsorption capacity Q_m can be determined with Langmuir and Sips isotherms. As expected, when compared to the whole mass of the filter, it was found to increase as the amount of additive increased (Table 1). The capacities varied from 2.6 mg g^{-1} to 12.2 mg g^{-1} for the 5–50 wt% filters. When the maximum capacity was calculated with respect to the amount of active additive, the maximum adsorption capacity decreased with the increasing amount of the additive. For example, for the 5 wt% filter, the capacity was 50.9 mg g^{-1}, while for the 30 wt% filter it was 30.7 mg g^{-1}. Thus, it could be concluded that the 5–20 wt% filters are more effective in adsorbing metals compared to the 30–50 wt% filters. The results indicate that the metal-rich leachate does not reach the adsorption sites of TP260 as easily when the amount of additive in the filter increases. It is difficult to determine whether this is related to the porosity and flow channels of the PA-TP260 filters or to the adsorption mechanism of TP260. Because the maximum adsorption capacities of the PA-TP260 filters were determined at a low pH of 0.15, they are generally lower than those reported for other aminophosphonate-based adsorbents at higher pH values (Table S8).[37,94,113–115]

Separation process

For separating elements of the NdFeB magnet into their own fractions, a process based on the PA-TP260 filters was developed according to the leaching, adsorption, and desorption studies wherein the underlying mechanics have been described in more detail. The process is depicted in Fig. 9, and the adsorption and desorption percentages as well as the amounts of the recovered elements (in mg) for each step of the process are presented in Table S9.

The process begins with the leaching step (step 1), after which Fe is removed from the leachate as described above (step

Table 1 Maximum adsorption capacities Q_m for the 5–50 wt% PA-TP260 filters calculated with respect to the mass of the filter (mg per g filter) and the amount of TP260 (mg per g TP260) in the filter

	Langmuir		Sips	
	Q_m (mg per g filter)	Q_m (mg per g TP260)	Q_m (mg per g filter)	Q_m (mg per g TP260)
5%	—	—	2.6 ± 0.2	50.9 ± 4.6
10%	7.6 ± 2.2	76.4 ± 21.8	5.8 ± 1.6	58.2 ± 15.7
20%	9.7 ± 2.4	48.6 ± 12.1	—	—
30%	9.12 ± 0.8	30.7 ± 2.5	—	—
40%	10.1 ± 0.5	25.2 ± 1.3	—	—
50%	12.2 ± 0.9	24.4 ± 1.7	—	—

This journal is © The Royal Society of Chemistry 2026

Open Access Article. Published on 09 April 2026. Downloaded on 4/30/2026 10:35:07 AM.
This article is licensed under a Creative Commons Attribution 3.0 Unported Licence.

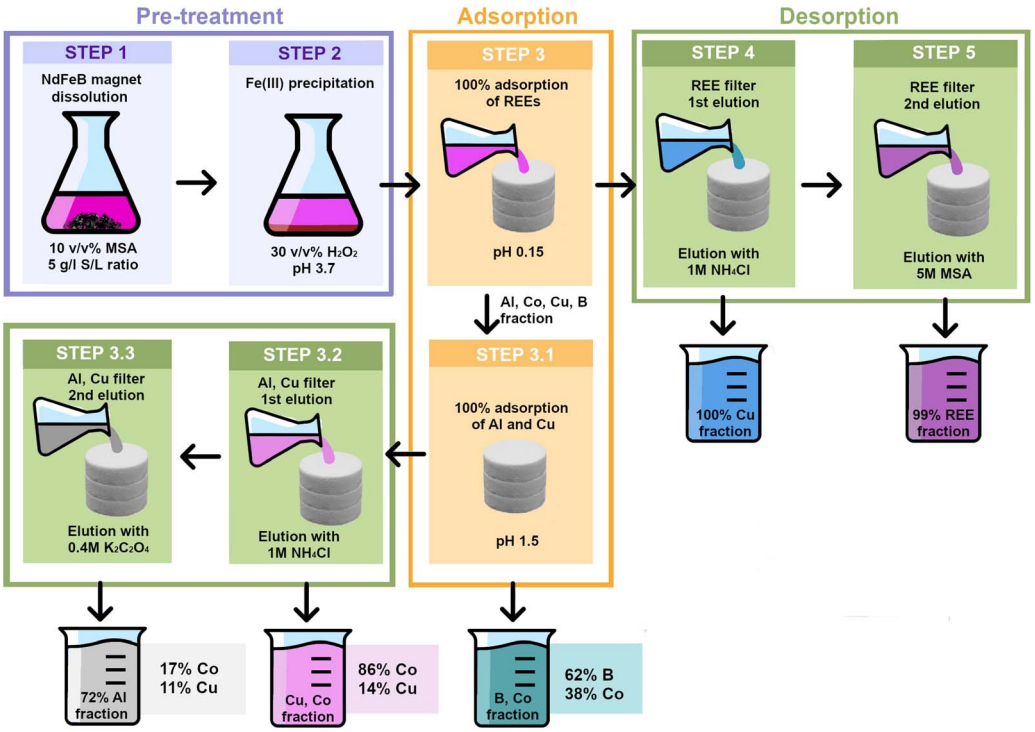

Fig. 9 Separation process for the investigated NdFeB magnet. The purity of each filtrate is given in percentages.

2). Then the pH of the leachate is set to 0.15 using 5% MSA, and REEs are completely adsorbed into the filter, while most of Al, Cu, Co, and B pass through the filters (step 3). At this low pH value, the aminophosphonic functional groups of TP260 remain mainly protonated while still having high affinity for REEs.[116] The filters containing REEs, and possibly a small amount of Co, Cu, and Al, are eluted with 1 M NH_4Cl to desorb weaker coordinated Cu from the filter (step 4). This step is followed by the elution of the filter with 30 ml of 5 M MSA, to recover REEs almost completely (>96%) from the filter into their own fraction with a purity of 99.4% (step 5). The pH of the filtrate, containing B, Al, Co, and Cu from step 3, is adjusted to 1.5 using 25% NH_4OH (step 3.1). The resulting solution is injected into the new set of filters to adsorb 100% of Al, 80% of Cu, and 50% of Co, whereas B remains in the solution, resulting in the filtrate containing 62% of B and 38% of Co (step 3.1). In this pH value the deprotonation degree of aminophosphate groups of TP260 is higher, and have better ability to adsorb Al, Cu, and Co from the solution.[37,116] The amount of Cu in the passing Co + B fraction is minimal (Table S9). The filters containing Al, Cu and Co is then eluted first with 30 ml of 1 M NH_4Cl (step 3.2), followed by 30 ml of 0.4 M potassium oxalate elution (step 3.3) to obtain a Co rich (step 3.2) fraction and Al rich (step 3.3) fraction, respectively.[117]

The results obtained for REE recovery in the above-described separation process are comparable to the best ones reported in the literature. For example, 99.9% pure REE fractions with a recovery rate of 99% have also been obtained in the separation processes of NdFeB magnets utilizing ionic liquids and oxalate precipitation.[17,118,119] In contrast to this, the 90% recovery of B in the developed process is lower by a small margin compared to that of alkali baking (90.3%)[120] and selective leaching (99.5%).[119] It is also worth mentioning that 99.9% of Fe with the purity of 97.6% was isolated in the preceding precipitation step, and Al, Co, and Cu were separated into their own less complex fractions in the subsequent separation steps. The latter is an important result because, apart from the separation of REEs, Fe, and B, previous studies have not extensively focused on the separation of other elements present in NdFeB magnets, to the best of our knowledge.[19–31] Overall, the obtained results highlight that precipitation combined with solid-phase adsorption, utilizing 3D printed filters and eco-friendly MSA, ammonium chloride, and potassium oxalate as eluents, is an efficient way to separate the elements from NdFBe magnets without strong mineral acids.

Conclusions

Separation of critical elements from the NdFeB magnet was studied with nylon-12 based 3D printed filters containing self-synthesised (**1**) or commercial amino-phosphonic acid (TP260) as an additive. In the adsorption tests, the PA-260 filters outperformed the PA-**1** filters as they separated REEs from Al, Co, Cu, and B at a low pH value of 0.15. The adsorption mechanism of the PA-TP260 filters were investigated using X-ray tomography and FTIR, while the fitting procedure to the adsorption isotherms were inconclusive. FTIR measurements revealed that (metal) ions present in the NdFeB magnet leachate coordinate to the phosphonate groups of the additive TP260, whereas, to the best of our knowledge, X-ray tomography was used for the

Open Access Article. Published on 09 April 2026. Downloaded on 4/30/2026 10:35:07 AM.
This article is licensed under a Creative Commons Attribution 3.0 Unported Licence.

first time to demonstrate that Nd is adsorbed by the additive, with minimal or no adsorption to the nylon-12 particles. Even though adsorption isotherms did not shed light on the adsorption mechanism, the maximum capacities of the 5–50 wt% PA-TP260 filters were extracted from them and they ranged from 7.6 ± 2.2 mg g^{-1} to 12.2 ± 0.9 mg g^{-1} (per mass of the filter) at pH 0.15. Finally, a separation process for separating REEs, B, Al, Co, and Cu was developed by combining MSA leaching, precipitation and solid phase extraction with eco-friendly MSA, ammonium chloride and potassium oxalate as eluents. The separation process resulted in the separated Fe and REE fractions with high purities of 97.6% and 99.4%, respectively, and four other fractions containing majority of Al, Co, Cu, and B. These results demonstrate that the separation of elements from the NdFeB magnet starting from the leaching step can also be performed without strong mineral acids like HNO_3, HCl, and H_2SO_4. Moreover, the PA-TP260 filters were thoroughly characterised with X-ray tomography. These studies showed that the filters are highly porous, robust, and fully reusable after 50 cycles, indicating their long-term performance ability in separation processes and applicability to industrial processes. Overall, this study paves the way for greener separation processes for secondary sources containing REEs as well as elements like Al, Co, Cu, or B.

Experimental details

Formaldehyde (36%) was purchased from VWR; phosphorous acid (99%) from Fluka Chemical Co.; dodecylamine (98%) from Merck, and methanesulfonic acid >98% from Thermo Scientific Chemicals. Nd_2O_3 (99.9%) was purchased from Sigma-Aldrich. 1000 mg per l ICP standard solutions for calibration were purchased from PerkinElmer. All chemicals were reagent grade and were used without further purification. [(Dodecylimino)bis(methylene)]bisphosphonic acid **1** was synthesized as described previously.[37] Aminophosphonic acid resin Lewatit TP260 was acquired from Lanxess. Metal concentrations were determined using a PerkinElmer ICP-OES Optima 8300 spectrometer and the filters were printed with a ShareBot Snow-White SLS 3D printer.

3D printing

FreeCAD v. 0.16 was used to design the model for the 3D printed filters. The model was further processed into two-dimensional, 0.1 mm thick layers using Slic3r v. 1.2.9. Powderous nylon-12 (particle size *ca.* 50 μm) was used as the polymer matrix in which 30 wt% of finely ground additive aminobisphosphonic acid **1** or 5–50 wt% of TP260 was mechanically mixed. The resulting powder mixtures were used as such to manufacture the respective 3D printed filters. For the powder containing additive **1**, print speeds between 1480 and 1600 mm s^{-1} were tested before selecting 1560 mm s^{-1} as the final speed; laser power was kept constant at 40% (of 14 W). The PA-TP260 filters were printed with laser power and speed of 50% (of 14 W) and 1480 mm s^{-1}. The printing temperature was kept constant (172 °C) for filters of additive **1** and PA-TP260 filters containing 50–30 wt% of the additive. The temperature was gradually lowered to 167 °C for 5 wt% filters to accommodate the increasing amount of nylon. The number of warming layers was kept at 40 for all prints, while the wait-time parameter was adjusted between prints (ranging between 450 and 900 seconds) to ensure the powder was evenly warmed up to prevent detaching layers or warping of the printed objects. The powder was sieved to remove any larger residues and mechanically mixed again between every print. The printed filters were thoroughly rinsed with water to remove any unsintered powder before using them in any experiments.

X-ray tomography

X-ray tomographic imaging was conducted at the Department of Physics of the University of Jyväskylä using two tomographs: an in-house-built X-ray tomographic scanner JTomo, and the Xradia MicroXCT-400 (Xradia, Concord, California, USA). Most of the tomographic scans in this study were performed using JTomo because it allows imaging of larger volumes relatively fast. The advantage of the Xradia MicroXCT-400 is its higher spatial resolution compared to the JTomo device, and it was used to study the micrometre level structure of PA-TP260 and PA-**1** in more detail in a small volume.

In the JTomo scans, the voltage and current of the microfocus X-ray tube (Hamamatsu L12161-07) were 40 kV and 200 μA, respectively, and no filtering of the X-ray spectrum was applied. The exposure time of the flat-panel detector (Teledyne Dalsa Shad-O-BOX, 7 MP) was two seconds. During the continuous rotation of 360°, either 1500 or 6000 projections (X-ray image at a certain rotation angle) were acquired. Most of the scans were performed with 1500 projections. However, when the changes in the grey scale distribution of the 3D image caused by the adsorption of Nd were assessed, the signal-to-noise ratio was improved by increasing the number of projections by a factor of four. The isotropic voxel size was set to 6.6 μm to study the micrometre level structure and still obtain a representative volume within the filter or powder sample. The image analysis for printed filters was performed in a volume of 9.6 mm × 9.6 mm × 4.8 mm. The filters imaged in this study were placed inside the syringe, which served as a sample holder. The same isotropic voxel size (6.6 μm) was used when the PA-TP260 powder sample was imaged and analysed in a volume of 4.3 mm × 6.5 mm × 9.9 mm.

In the Xradia MicroXCT-400 scans, the voltage and current of the microfocus X-ray tube (Hamamatsu L9421-02) were 40 kV and 100 μA, respectively, and no filtering of the X-ray spectrum was applied. The exposure time of the CCD camera (Andor DW436-BV-550, 4 MP) was 15 seconds. Two thousand projections were acquired during the rotation of 184°. MicroXCT-400 is an X-ray microscope in which a scintillator is coupled to the CCD camera *via* an optical microscope. Here, 20× magnification was used to achieve an isotropic voxel size of 0.6 μm. Small pieces (1 mm × 1 mm × 4 mm) were cut from the printed PA-TP260 and PA-**1** filters for the scans.

In both cases, the 3D tomographic image was reconstructed using the Feldkamp–Davis–Kress formulation of the filtered back-projection algorithm[121] in the pi2 software. The noise in all

Open Access Article. Published on 09 April 2026. Downloaded on 4/30/2026 10:35:07 AM. This article is licensed under a Creative Commons Attribution 3.0 Unported Licence.

the tomographic images was reduced by applying bilateral filtering in 3D. Pore volume and material segmentation were performed using the Otsu thresholding method[122] for printed filters. For the PA-TP260 powder sample, the exact same threshold as for the corresponding printed filter was applied to ensure the comparability of the particle size distribution results (Fig. S4). After segmentation, the binary image containing only two voxel values/colours (black for air and white for the filter material) was used for the image analysis. The pore size distribution was estimated based on statistical binning of the local thickness map of the image.[123] The value of a voxel in the thickness map is the diameter of the largest sphere that fits into the pore volume and contains the voxel, and therefore encodes the local pore size. For particle size distribution measurement, individual particles were segmented using the watershed segmentation algorithm.[124] The size of an individual particle was estimated by determining the radius of the smallest sphere containing all the voxels in the particle.[125]

Furthermore, the total surface area between the filter material and air in the printed filter was measured using the marching cubes algorithm.[126] In addition, the connected porosity was calculated from the total pore volume that was reachable from the outside of the filter with a flood fill algorithm. All image analyses were performed using the pi2 software.[127] The error estimates of the image analysis results are based on repeating the analysis workflow using slightly different parameter values in the analysis methods.

Scanning near-field optical microscopy (SNOM)

Broadband scattering-SNOM imaging and nano-FTIR measurements were performed using a NeaSNOM™ instrument (Attocube Systems AG) equipped with a tunable broadband mid-infrared laser source (Toptica Photonics AG). Nano-FTIR phase (φ_n) and amplitude spectra (A_n) were measured in the 1000–1800 cm^{-1} spectral range as a function of harmonic demodulation orders ($n\times\ \Omega$, where $n = 1,\ldots,4$). The second harmonic phase ($\varphi_2 = O_{2P}$) was chosen to represent the near-field absorption spectrum. Pt/Ir-coated AFM tips (Arrow-NCPt, Nanoworld® AG) with a fundamental mechanical frequency ($\Omega \approx 275$ kHz) were used in the measurements.

Spectra were recorded using a liquid nitrogen-cooled HgCdTe (MCT) detector, with a spectral resolution of 16 cm^{-1}, a pixel integration time of 20 ms, and averaged over 10 scans to improve signal quality. Contact tapping amplitude of 60 nm was used in the acquisition of the spectra from sample surfaces. All nano-FTIR spectra are referenced to an Au background and baseline-corrected using software packages neaPLOT and OriginPro 2017.

Magnet leaching

Methanesulfonic acid (MSA) was used for leaching the grounded magnets with 10–100 vol% MSA solutions. The temperature was kept at 60 °C for 24 hours and S/L ratio of 5 g l^{-1} was used by weighing 25 mg of the magnet to 5 ml of the acid. The undissolved material was filtered, and the solution was diluted to 100 ml with ultrapure water and adjusted with MSA to obtain 5% MSA. The concentrations of each metal were measured with ICP-OES. For accurate determination of the percentages of dissolved ions, total dissolution was performed by dissolving 25 mg of the magnet in 5 ml of aqua regia which was similarly filtered and diluted to 100 ml.

Iron precipitation

Iron was removed from the magnet leachate by oxidizing Fe(II) to Fe(III) with an excess of H_2O_2 and adjusting the pH to 4 using 25% NH_4OH. More than 99% of Fe precipitated from the leachate, with only insignificant amounts of other elements present.

Adsorption and desorption tests

For the adsorption tests, the pH of the NdFeB magnet solution was set to 1–4 with 25% NH_4OH. A 40 ml of the solution was withdrawn into a 60 ml syringe that was attached to a syringe pump and the flow rate was set to 90 ml h^{-1}. The solution was injected through the three stacked 3D printed filters. pH was measured before and after the adsorption process to confirm the stability of adsorption conditions. Adsorption percentages and the amounts of desorbed metals were determined with a PerkinElmer ICP-OES Optima 8300 by measuring the concentrations of elements in the solution before and after passing the solutions through the 3D printed metal filters. Adsorption percentages were calculated with eqn (1)

$$\text{Adsorption}\% = \frac{c_i - c_f}{c_i} \times 100\% \quad (1)$$

where c_i and c_f are the element concentrations (mg l^{-1}) before and after adsorption tests, respectively.

Desorption of the metals from the used filters was studied with 3 M and 5 M MSA as well as with 6 M HNO_3 by passing 30 ml of the acid through the filters with a flow rate of 15 ml h^{-1}. Desorption percentages were calculated with eqn (2)

$$\text{Desorption}\% = \frac{C_d \times V}{m_a} \times 100\% \quad (2)$$

in which C_d is the concentration of desorbed metals (mg l^{-1}), V is the volume of the acid passed through (l), and m_a is the adsorbed amount of metals in the filter (mg).

Adsorption–desorption cycles

The structural changes in the filter during 50 adsorption–desorption cycles were investigated with X-ray tomography. 9 ml of the simulated NdFeB solution containing 22 mg l^{-1} of Nd, 3.5 mg l^{-1} of Dy, 8 mg l^{-1} of Pr, 2 mg l^{-1} of Al, 1.5 mg l^{-1} of B and $\leq$1 mg l^{-1} of Co, Sm, Tb, Ho, and Cu was injected to one filter at pH 0.15 with a flow rate of 90 ml h^{-1}. The elements were desorbed from the filter with 20 ml of 5 M MSA, except for the first five cycles where 3 M MSA was used, using the flow rate of 15 ml h^{-1}. Elemental concentrations were measured with an Optima ICP-OES 8300.

Adsorption isotherms

Nd solutions containing 50, 100, 250, 500, 750 and 1000 mg l^{-1} of Nd were prepared from Nd_2O_3. 10 ml of each solution was passed through one filter containing 5 wt%, 10 wt%, 20 wt%, 30 wt%, 40 wt%, or 50 wt% of the additive TP260 using a flow

Open Access Article. Published on 09 April 2026. Downloaded on 4/30/2026 10:35:07 AM. This article is licensed under a Creative Commons Attribution 3.0 Unported Licence.

rate of 90 ml h^{-1}. Langmuir,[106] Freundlich,[107] and Sips[108] adsorption isotherm models were then fitted to the experimental data points. All tests were performed in triplicate, and the concentration of Nd was measured with an Optima ICP-OES 8300. Langmuir isotherm[106] is expressed as

$$q_e = \frac{q_m b C_e}{1 + b C_e} \quad (3)$$

in which q_m is the maximum adsorption capacity (mg g^{-1}), b is the Langmuir constant (l mg^{-1}), q_e is the equilibrium loading (mg g^{-1}), and C_e is the concentration at equilibrium (mg l^{-1}). Freundlich adsorption isotherm[107] is expressed as

$$q_e = K_f C_e^{\frac{1}{n}} \quad (4)$$

in which K_f is the Freundlich constant (l mg^{-1}) and n is a constant indicating adsorption intensity. Sips isotherm[108] is expressed as

$$q_e = \frac{q_m K_s C_e^{n_s}}{1 + b C_e^{n_s}} \quad (5)$$

in which K_s (L^{n_s} mg^{-n_s}) and n_s are the Sips constants.

Separation process

For the recovery cycle, 10 ml of the NdFeB leachate was first passed through the three stacked PA-TP260 filters at pH 0.15 using a flow rate of 90 ml h^{-1}. The pH of the filtrate, which passed through the first set of filters, was adjusted to 1.5 with 25% NH_4OH and passed through the second sets of filters with the same flow rate. The first set of filters was eluted with 30 ml of 1 M NH_4Cl with a flow rate of 15 ml h^{-1} followed by 30 ml of 5 M MSA. The second set of filters was eluted first with 30 ml of 1 M NH_4Cl followed by 30 ml of 0.4 M potassium oxalate. All the concentrations from the initial solutions and filtrates were determined with an Optima ICP-OES 8300. For further details see Fig. 9 as well as the Results and discussion section.

Author contributions

Emilia J. Virtanen: writing – review & editing, writing – original draft, visualization, validation, investigation, formal analysis, conceptualization. Janne Yliharju: formal analysis, investigation, visualization, writing – original draft, writing – review & editing. Esa Kukkonen: writing – review & editing, resources, investigation. Tia Christiansen: investigation. Eero Hulkko: formal analysis, investigation. Minnea Tuomisto: formal analysis, investigation. Arttu Miettinen: writing – review & editing, supervision, funding acquisition, investigation, resources. Mika Lastusaari: supervision, funding acquisition. Ari Väisänen: writing – review & editing, supervision, funding acquisition, conceptualization. Jani O. Moilanen: writing – review & editing, writing – original draft, visualization, supervision, resources, project administration, funding acquisition, data curation, conceptualization.

Conflicts of interest

Intellectual property related to the technology described in this article is covered by PCT Patent Application No. 20246367.[128]

Data availability

Supplementary information: additional figures and tables referenced in the text, further discussion related to the FTIR spectra, as well as the original data presented in the figures of this article. See DOI: https://doi.org/10.1039/d5ta09708h.

Acknowledgements

We thank the University of Jyväskylä, the Research Council of Finland (project 338733), the Technology Industries of Finland Centennial Foundation and Jane and Aatos Erkko Foundation for their financial support. The authors also thank Lanxess for providing Lewatit TP260 for us.

References

1 A. Kumari and S. K. Sahu, *Sep. Purif. Technol.*, 2023, **317**, 123527.
2 Y. Yang, A. Walton, R. Sheridan, K. Güth, R. Gauß, O. Gutfleisch, M. Buchert, B.-M. Steenari, T. Van Gerven, P. T. Jones and K. Binnemans, *J. Sustainable Metall.*, 2017, **3**, 122–149.
3 M. Pan, P. Zhang, X. Li, H. Ge, Q. Wu, Z. Jiao and T. Liu, *J. Rare Earths*, 2010, **28**, 399–402.
4 T. Elwert, D. Goldmann, F. Roemer and S. Schwarz, *J. Sustainable Metall.*, 2017, **3**, 108–121.
5 C.-C. Mo, C.-C. Kuan, Y.-H. Wang, Y.-S. Lu, T.-W. Chang, W.-Y. Liao, T.-H. Fang, M.-C. Tsai and C.-C. Huang, *J. Magn. Magn. Mater.*, 2023, **578**, 170808.
6 S. Bobba, S. Carrara, J. Huisman, F. Mathieux and C. Pavel, *Critical Raw Materials for Strategic Technologies and Sectors in the EU – A Foresight Study*, 2020.
7 C. P. Couto, J. J. M. M. van de Ven, Y. Yang and S. T. Abrahami, *Sustainable Mater.Technol.*, 2024, **41**, e01041.
8 A. Lixandru, P. Venkatesan, C. Jönsson, I. Poenaru, B. Hall, Y. Yang, A. Walton, K. Güth, R. Gauß and O. Gutfleisch, *Waste Manage.*, 2017, **68**, 482–489.
9 T. J. McIntyre and J. J. Harter, *US Pat.*, US11230752B2, 2022.
10 T. R. Simon, L. Cong, Y. Zhai, Y. Zhu and F. Zhao, *Procedia CIRP*, 2018, **69**, 916–920.
11 M. Kaya, *Curr. Opin. Green Sustainable Chem.*, 2024, **46**, 100884.
12 S. Shirayama and T. H. Okabe, *Metall. Mater. Trans. B*, 2018, **49**, 1067–1077.
13 B. Liu, N. Zhu, Y. Li, P. Wu, Z. Dang and Y. Ke, *Process Saf. Environ. Prot.*, 2019, **124**, 317–325.
14 J.-P. Harvey, W. Courchesne, M. D. Vo, K. Oishi, C. Robelin, U. Mahue, P. Leclerc and A. Al-Haiek, *MRS Energy Sustainability*, 2022, **9**, 212–247.
15 Z. Liu, H. Zhou, W. Li, X. Luo, J. Wang and F. Liu, *Sep. Purif. Technol.*, 2022, **282**, 119795.
16 J. Niskanen, M. Lahtinen and S. Perämäki, *Cleaner Eng. Technol.*, 2022, **10**, 100544.
17 D. Dupont and K. Binnemans, *Green Chem.*, 2015, **17**, 2150–2163.

 This journal is © The Royal Society of Chemistry 2026

Open Access Article. Published on 09 April 2026. Downloaded on 4/30/2026 10:35:07 AM. This article is licensed under a Creative Commons Attribution 3.0 Unported Licence.

18 E. Yamada, H. Murakami, S. Nishihama and K. Yoshizuka, *Sep. Purif. Technol.*, 2018, **192**, 62–68.
19 P. Sun, K. Huang, W. Song, Z. Gao and H. Liu, *Ind. Eng. Chem. Res.*, 2018, **57**, 16934–16943.
20 J. Xu, R. Koivula, W. Zhang, E. Wiikinkoski, S. Hietala and R. Harjula, *Hydrometallurgy*, 2018, **175**, 170–178.
21 J. Xu, S. Virolainen, W. Zhang, J. Kuva, T. Sainio and R. Koivula, *Chem. Eng. J.*, 2018, **351**, 832–840.
22 B. E. Cole, I. B. Falcones, T. Cheisson, B. C. Manor, P. J. Carroll and E. J. Schelter, *Chem. Commun.*, 2018, **54**, 10276–10279.
23 N. Maât, V. Nachbaur, R. Lardé, J. Juraszek and J.-M. Le Breton, *ACS Sustainable Chem. Eng.*, 2016, **4**, 6455–6462.
24 A. Ding, C. Liu, X. Zhang, L. Lei and C. Xiao, *Environ. Sci. Technol.*, 2022, **56**, 4404–4412.
25 B. Dewulf, N. K. Batchu and K. Binnemans, *ACS Sustainable Chem. Eng.*, 2020, **8**, 19032–19039.
26 H. Onoda and A. Iinuma, *J. Environ. Chem. Eng.*, 2020, **8**, 104083.
27 Y. Yang, Y. Qin, T. Wang, Y. Zhang, T. Shi, J. Li, H. Xu, Z. Xia, H. Sun and Z. Zhao, *Sep. Purif. Technol.*, 2023, **311**, 123185.
28 J. A. Bogart, C. A. Lippincott, P. J. Carroll and E. J. Schelter, *Angew. Chem., Int. Ed.*, 2015, **54**, 8222–8225.
29 J. J. M. Nelson, T. Cheisson, H. J. Rugh, M. R. Gau, P. J. Carroll and E. J. Schelter, *Commun. Chem.*, 2020, **3**, 1–6.
30 T. Cheisson, B. E. Cole, B. C. Manor, P. J. Carroll and E. J. Schelter, *ACS Sustainable Chem. Eng.*, 2019, **7**, 4993–5001.
31 J. G. O'Connell-Danes, B. Ozen Ilik, E. E. Hull, B. T. Ngwenya, C. A. Morrison and J. B. Love, *ACS Sustainable Chem. Eng.*, 2024, **12**, 9301–9305.
32 Ł. Stala, J. Ulatowska and I. Polowczyk, *Water Res.*, 2021, **203**, 117523.
33 D. Kołodyńska, Z. Hubicki and M. Gęca, *Ind. Eng. Chem. Res.*, 2008, **47**, 3192–3199.
34 M. Hermassi, M. Granados, C. Valderrama, N. Skoglund, C. Ayora and J. L. Cortina, *J. Cleaner Prod.*, 2022, **379**, 134742.
35 M. Hermassi, M. Granados, C. Valderrama, C. Ayora and J. L. Cortina, *J. Environ. Chem. Eng.*, 2021, **9**, 105906.
36 M. Hermassi, M. Granados, C. Valderrama, C. Ayora and J. L. Cortina, *Sci. Total Environ.*, 2022, **810**, 152258.
37 E. J. Virtanen, E. Kukkonen, J. Yliharju, M. Tuomisto, J. Frimodig, K. Kinnunen, E. Lahtinen, M. M. Hänninen, A. Väisänen, M. Haukka and J. O. Moilanen, *Sep. Purif. Technol.*, 2025, **353**, 128599.
38 N. Reynier, M. Courchesne, J. Basque, C. Laviolette, A. Demers and D. Larivière, *Miner. Eng.*, 2022, **175**, 107284.
39 LEWATIT-MonoPlus-TP-260, https://lanxess.com/en-US/Products-and-Brands/Products/l/LEWATIT–MonoPlus-TP-260, accessed June 10, 2024.
40 A. Kadous, M. A. Didi and D. Villemin, *J. Radioanal. Nucl. Chem.*, 2011, **288**, 553–561.
41 K. Suwannahong, J. Sripirom, C. Sirilamduan, V. Thathong, T. Kreetachart, P. Panmuang, A. Deepatana, S. Punbut, S. Wongcharee and H. Hamad, *Adsorpt. Sci. Technol.*, 2022, **2022**, 5009124.
42 N. H. Mohd Yusoff, L.-R. Irene Teo, S. J. Phang, V.-L. Wong, K. H. Cheah and S.-S. Lim, *Chem. Eng. J.*, 2022, **429**, 132311.
43 K. Ibebunjo, Y. El Ouardi, J. Kwame Bediako, A. Iurchenkova and E. Repo, *Chem. Eng. Sci.*, 2024, **286**, 119664.
44 R. Li, S. Yuan, W. Zhang, H. Zheng, W. Zhu, B. Li, M. Zhou, A. Wing-Keung Law and K. Zhou, *ACS Appl. Mater. Interfaces*, 2019, **11**, 40564–40574.
45 E. Lahtinen, E. Kukkonen, V. Kinnunen, M. Lahtinen, K. Kinnunen, S. Suvanto, A. Väisänen and M. Haukka, *ACS Omega*, 2019, **4**, 16891–16898.
46 E. Lahtinen, M. M. Hänninen, K. Kinnunen, H. M. Tuononen, A. Väisänen, K. Rissanen and M. Haukka, *Adv. Sustainable Syst.*, 2018, **2**, 1800048.
47 E. Lahtinen, L. Kivijärvi, R. Tatikonda, A. Väisänen, K. Rissanen and M. Haukka, *ACS Omega*, 2017, **2**, 7299–7304.
48 Y. Miao, W. Peng, W. Wang, Y. Cao, H. Li, L. Chang, Y. Huang, G. Fan, H. Yi, Y. Zhao and T. Zhang, *Sep. Purif. Technol.*, 2022, **283**, 120176.
49 H. Nasser Abdelhamid, S. Sultan and A. P. Mathew, *Chem. Eng. J.*, 2023, **468**, 143567.
50 S. Ma, S. Fu, H. Yang, P. He, Z. Sun, X. Duan, D. Jia, P. Colombo and Y. Zhou, *J. Cleaner Prod.*, 2024, **437**, 140599.
51 F. Song, W. Chen, Y. Guo, Z. Wang, Q. Chen, Q. Zhao, T. Tian, Q. Chen, M. Zhang and B. Liu, *Sep. Purif. Technol.*, 2024, **340**, 126629.
52 C. A. Grande, R. Blom, V. Middelkoop, D. Matras, A. Vamvakeros, S. D. M. Jacques, A. M. Beale, M. Di Michiel, K. Anne Andreassen and A. M. Bouzga, *Chem. Eng. J.*, 2020, **402**, 126166.
53 S. N. Sluijter, J. Boon, J. James, S. Krishnamurthy, A. Lind, R. Blom, K. A. Andreassen, A. M. Cormos, V. C. Sandu and R. de Boer, *Int. J. Greenhouse Gas Control*, 2021, **112**, 103512.
54 O. Halevi, T.-Y. Chen, P. See Lee, S. Magdassi and J. A. Hriljac, *RSC Adv.*, 2020, **10**, 5766–5776.
55 M. Rodas Ceballos, F. González Serra, J. M. Estela, V. Cerdà and L. Ferrer, *Talanta*, 2019, **196**, 510–514.
56 N. P. F. Gonçalves, E. F. da Silva, L. A. C. Tarelho, J. A. Labrincha and R. M. Novais, *J. Hazard. Mater.*, 2024, **462**, 132718.
57 K. G. Oliveira, R. Botti, V. Kavun, A. Gafiullina, G. Franchin, E. Repo and P. Colombo, *Catal. Today*, 2022, **390–391**, 57–68.
58 C. Calderilla, F. Maya, V. Cerdà and L. O. Leal, *Talanta*, 2018, **184**, 15–22.
59 S. Giret, Y. Hu, N. Masoumifard, J.-F. Boulanger, E. Juère, F. Kleitz and D. Larivière, *ACS Appl. Mater. Interfaces*, 2018, **10**, 448–457.
60 Y. Hu, L. C. Misal Castro, E. Drouin, J. Florek, H. Kählig, D. Larivière, F. Kleitz and F.-G. Fontaine, *ACS Appl. Mater. Interfaces*, 2019, **11**, 23681–23691.
61 J. Frimodig and M. Haukka, *Environ. Sci.: Adv.*, 2023, **2**, 1739–1745.

Open Access Article. Published on 09 April 2026. Downloaded on 4/30/2026 10:35:07 AM. This article is licensed under a Creative Commons Attribution 3.0 Unported Licence.

62 T. Luukkonen, J. Yliniemi, H. Sreenivasan, K. Ohenoja, M. Finnilä, G. Franchin and P. Colombo, *Sci. Rep.*, 2020, **10**, 7233.
63 N. P. F. Gonçalves, S. M. Olhero, J. A. Labrincha and R. M. Novais, *J. Cleaner Prod.*, 2023, **383**, 135315.
64 H. Goodarzi Hosseinabadi, D. Nieto, A. Yousefinejad, H. Fattel, L. Ionov and A. K. Miri, *Appl. Mater. Today*, 2023, **30**, 101721.
65 S. Kulomäki, E. Lahtinen, S. Perämäki and A. Väisänen, *Anal. Chim. Acta*, 2019, **1092**, 24–31.
66 N. R. Rodriguez, B. Grymonprez and K. Binnemans, *Ind. Eng. Chem. Res.*, 2021, **60**, 10319–10326.
67 C. Chang, S. Yang, Y. Li, C. Xiang, H. Wang, S. Liu, T. Luo and Y. Chen, *Sep. Purif. Technol.*, 2023, **306**, 122592.
68 L. Gijsemans, F. Forte, B. Onghena and K. Binnemans, *RSC Adv.*, 2018, **8**, 26349–26355.
69 F. Forte, L. Yurramendi, J. Luis Aldana, B. Onghena and K. Binnemans, *RSC Adv.*, 2019, **9**, 1378–1386.
70 X. Zhang, J. Guan, Y. Guo, Y. Cao, J. Guo, H. Yuan, R. Su, B. Liang, G. Gao, Y. Zhou, J. Xu and Z. Guo, *Environ. Prog. Sustainable Energy*, 2017, **36**, 873–878.
71 L. Mester, A. A. Govyadinov and R. Hillenbrand, *Nanophotonics*, 2022, **11**, 377–390.
72 J. M. Larson, H. A. Bechtel and R. Kostecki, *Adv. Funct. Mater.*, 2024, **34**, 2406643.
73 T. Palden, B. Onghena, M. Regadío and K. Binnemans, *Green Chem.*, 2019, **21**, 5394–5404.
74 N. Rodriguez Rodriguez, B. Onghena and K. Binnemans, *ACS Sustainable Chem. Eng.*, 2019, **7**, 19807–19815.
75 D. D. München, A. M. Bernardes and H. M. Veit, *J. Sustainable Metall.*, 2018, **4**, 288–294.
76 S. S. Behera and P. K. Parhi, *Sep. Purif. Technol.*, 2016, **160**, 59–66.
77 E. Emil-Kaya, B. Polat, S. Stopic, S. Gürmen and B. Friedrich, *RSC Adv.*, 2023, **13**, 1320–1332.
78 J. Park, in *2020 11th International Renewable Energy Congress (IREC)*, IEEE, Hammamet, Tunisia, 2020, pp. 1–6.
79 A. G. Belous, E. V. Pashkova, V. A. Elshanskii and V. P. Ivanitskii, *Inorg. Mater.*, 2000, **36**, 343–351.
80 B. Vaziri Hassas, M. Rezaee and S. V. Pisupati, *Chem. Eng. J.*, 2020, **399**, 125716.
81 X. Hu, H. Yang, K. Tan, S. Hou, J. Cai, X. Yuan, Q. Lan, J. Cao and S. Yan, *J. Environ. Chem. Eng.*, 2022, **10**, 106974.
82 E. J. Virtanen, S. Perämäki, K. Helttunen, A. Väisänen and J. O. Moilanen, *ACS Omega*, 2021, **6**, 23977–23987.
83 P. N. Nesterenko, M. J. Shaw, S. J. Hill and P. Jones, *Microchem. J.*, 1999, **62**, 58–69.
84 R. Panda, F. Flecken, C. Papke, C. E. Anson, T. Grell and S. Hanf, *ACS Omega*, 2026, **11**, 15462–15475.
85 K. P. Kepp, *Inorg. Chem.*, 2016, **55**, 9461–9470.
86 K. Ohkubo, S. C. Menon, A. Orita, J. Otera and S. Fukuzumi, *J. Org. Chem.*, 2003, **68**, 4720–4726.
87 J. R. Gaffen, J. N. Bentley, L. C. Torres, C. Chu, T. Baumgartner and C. B. Caputo, *Chem*, 2019, **5**, 1567–1583.
88 R. R. Golwankar, T. D. I. Curry, C. J. Paranjothi and J. D. Blakemore, *Inorg. Chem.*, 2023, **62**, 9765–9780.
89 J. N. Bentley, S. A. Elgadi, J. R. Gaffen, P. Demay-Drouhard, T. Baumgartner and C. B. Caputo, *Organometallics*, 2020, **39**, 3645–3655.
90 G. D. Z. Williams, P. Nativ and A. Vengosh, *Sci. Adv.*, 2025, **11**, eadw3268.
91 S. D. Alexandratos, *Ind. Eng. Chem. Res.*, 2009, **48**, 388–398.
92 F. de Dardel and T. V. Arden, in *Ullmann's Encyclopedia of Industrial Chemistry*, John Wiley & Sons, Ltd, 2008.
93 R. Thapa, T. Nissinen, P. Turhanen, J. Määttä, J. Vepsäläinen, V.-P. Lehto and J. Riikonen, *Microporous Mesoporous Mater.*, 2020, **296**, 109980.
94 E. A. Imam, A. I. Hashem, X. Lu, A. A. Tolba, M. G. Mahfouz, J. Xin, I. E.-T. El-Sayed, S. I. Mohamady, A. A. S. Ahmed, A. A. Galhoum and E. Guibal, *Colloids Surf., A*, 2024, **685**, 133339.
95 X. Zheng, E. Liu, F. Zhang, Y. Yan and J. Pan, *Green Chem.*, 2016, **18**, 5031–5040.
96 R. Thapa, A. Rahmani, P. Turhanen, A. Taskinen, T. Nissinen, R. Neitola, J. Vepsäläinen, V.-P. Lehto and J. Riikonen, *Sep. Purif. Technol.*, 2021, **272**, 118913.
97 Z. Hubicki, M. Gęca and D. Kołodyńska, *Environ. Technol.*, 2011, **32**, 805–816.
98 R. Kiefer and W. H. Höll, *Ind. Eng. Chem. Res.*, 2001, **40**, 4570–4576.
99 S. K. Sahni, R. Van Bennekom and J. Reedijk, *Polyhedron*, 1985, **4**, 1643–1658.
100 S. A. Ali, I. B. Rachman and T. A. Saleh, *Chem. Eng. J.*, 2017, **330**, 663–674.
101 A. Givan, A. Loewenschuss and C. J. Nielsen, *J. Mol. Struct.*, 2005, **748**, 77–90.
102 P. Larkin, *Infrared and Raman Spectroscopy: Principles and Spectral Interpretation*, Elsevier, San Diego, United States, 2011.
103 V. D. Maiorov, G. I. Voloshenko and N. B. Librovich, *Russ. J. Phys. Chem. B*, 2011, **5**, 271–277.
104 B. C. Barja, J. Herszage and M. dos Santos Afonso, *Polyhedron*, 2001, **20**, 1821–1830.
105 W. Zou, N. Hunter and M. V. Swain, *J. Dent. Res.*, 2011, **90**, 18–30.
106 I. Langmuir, *J. Am. Chem. Soc.*, 1916, **38**, 2221–2295.
107 H. Freundlich and G. Losev, *Z. Phys. Chem.*, 1907, **59U**, 284–312.
108 R. Sips, *J. Chem. Phys.*, 1948, **16**, 490–495.
109 Q. Hu, R. Lan, L. He, H. Liu and X. Pei, *J. Environ. Manage.*, 2023, **329**, 117104.
110 A. Sraidi, S. Ait hak, S. Kounbach, K. Khaless and R. Benhida, *J. Mol. Liq.*, 2024, **402**, 124758.
111 B. Esma, A. Omar and D. M. Amine, *J. Radioanal. Nucl. Chem.*, 2014, **299**, 439–446.
112 D. Kołodyńska, D. Fila and Z. Hubicki, *Environ. Res.*, 2020, **191**, 110171.
113 K. Burdzy, Y. Ju and D. Kołodyńska, *Chem. Eng. J.*, 2023, **461**, 142059.
114 A. A. Galhoum, T. Akashi, M. Linnolahti, J. T. Hirvi, A. G. Al-Sehemi, A. Kalam and E. Guibal, *React. Funct. Polym.*, 2022, **180**, 105389.

 This journal is © The Royal Society of Chemistry 2026

Open Access Article. Published on 09 April 2026. Downloaded on 4/30/2026 10:35:07 AM.
This article is licensed under a Creative Commons Attribution 3.0 Unported Licence.

115 A. R. Elsalamouny, O. A. Desouky, S. A. Mohamed, A. A. Galhoum and E. Guibal, *Int. J. Biol. Macromol.*, 2017, **104**, 963–968.
116 E. J. Virtanen, S. Perämäki, K. Helttunen, A. Väisänen and J. O. Moilanen, *ACS Omega*, 2021, **6**, 23977–23987.
117 S. Virolainen, T. Wesselborg, A. Kaukinen and T. Sainio, *Hydrometallurgy*, 2021, **202**, 105602.
118 A. Kumari, M. K. Sinha, S. Pramanik and S. K. Sahu, *Waste Manage.*, 2018, **75**, 486–498.
119 F. Liu, A. Porvali, J. Wang, H. Wang, C. Peng, B. P. Wilson and M. Lundström, *Miner. Eng.*, 2020, **145**, 106097.
120 M. A. R. Önal, S. Riaño and K. Binnemans, *Hydrometallurgy*, 2020, **191**, 105213.
121 L. A. Feldkamp, L. C. Davis and J. W. Kress, *J. Opt. Soc. Am. A*, 1984, **1**, 612–619.
122 N. Otsu, *IEEE Trans. Syst. Man Cybern.*, 1979, **9**, 62–66.
123 A. Miettinen, E. Borisova, M. Stampanoni and G. Lovric, *Comput. Vision Image Understanding*, 2025, **260**, 104443.
124 S. Beucher and F. Meyer, in *Mathematical Morphology in Image Processing*, CRC Press, 2018, pp. 433–481.
125 E. Welzl, in *New Results and New Trends in Computer Science*, ed. H. Maurer, Springer, Berlin, Heidelberg, 1991, pp. 359–370.
126 W. E. Lorensen and H. E. Cline, in *Seminal Graphics: Pioneering Efforts that Shaped the Field, Volume 1*, Association for Computing Machinery, New York, NY, USA, 1998, vol. 1, pp. 347–353.
127 pi2, https://github.com/arttumiettinen/pi2, accessed September 2025.
128 E. Virtanen, J. Moilanen, A. Väisänen and E. Kukkonen, Method for recovering rare earth elements, *PCT Pat.*, application No. 20246367, 2025, 1–24.